IEEE Robotics and Automation Letters (RAL) paper presented at
2024 IEEE/RSJ International Conference on Intelligent Robots and Systems (IROS)
October 14-18, 2024. Abu Dhabi, UAE

Hyperboloidal Pneumatic Artificial Muscle with Braided Straight Fibers

Masahiro Watanabe, Kenjiro Tadakuma, and Satoshi Tadokoro

***Abstract*— This paper introduces the development and analysis of a hyperboloidal pneumatic artificial muscle (h-PAM) utilizing braided straight fibers, aimed at overcoming the limitations of traditional pneumatic artificial muscles (PAMs). The novel design features a hyperboloidal rubber tube coupled with a braided shell of straight fibers, enhancing both contraction performance and flexibility, a significant advantage particularly for shorter muscles. Through deformation simulations, we have demonstrated that critical performance metrics such as contraction ratio, radius expansion ratio, and contraction force can be effectively tailored by adjusting the height-to-radius ratio and the fiber's offset angle. The fabricated h-PAM prototype's performance was evaluated, showcasing its capability for contraction and flexibility even in compact forms, thus highlighting its potential as an actuator in soft robotics applications.**

***Index Terms*—Hydraulic/Pneumatic Actuators, Modeling, Control, and Learning for Soft Robots, Soft Sensors and Actuators.**

I. Introduction

Pneumatic actuators, typically in the form of cylinders, are extensively utilized in applications such as factory automation and automatic door systems. These actuators offer the advantage of adjusting force and velocity through simple modifications of air pressure and flow. Notably, they maintain consistent performance in environments characterized by dust, high humidity, and strong magnetic fields. Additionally, pneumatic actuators are capable of sustaining force without continuous energy consumption.

Recently, pneumatic artificial muscles (PAMs) have gained widespread use in the field of soft robotics [1][2]. PAMs attract researchers as their lightweight design, high power output, compliant behavior, and flexibility. These muscles typically comprise thin membranes, including a braided shell and an inner rubber tube. Inflating these muscles increases their volume, causing radial expansion and axial contraction of the tube. Such distinctive features offer considerable potential for various applications, including human-assistive wearable devices, continuum robots for manipulators and soft mobile robots.

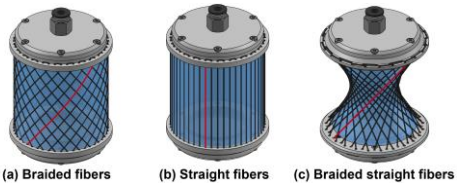

Fig. 1 Pneumatic artificial muscles reinforced by fibers. Illustration showing a single inextensible fiber in each PAM, marked with red lines.

Manuscript received: November 15, 2023; Revised February 2, 2024; Accepted February 29, 2024. This paper was recommended for publication by Editor Cecilia Laschi upon evaluation of the Associate Editor and Reviewers' comments.This work was supported by the Fluid Power Technology Promotion Foundation. [1]Masahiro Watanabe and Kenjiro Tadakuma are with the Tough Cyberphysical AI Research Center, Tohoku University, Sendai, 980-8579 Japan (e-mail: watanabe.masahiro@rm.is.tohoku.ac.jp; tadakuma@rm.is.tohoku.ac.jp). [2]Satoshi Tadokoro is with the Graduate School of Information Sciences, Tohoku University, Sendai, 980-8579 Japan (email: tadokoro@rm.is.tohoku.ac.jp)

Digital Object Identifier (DOI): see top of this page.


Fig. 2 Prototype of hyperboloidal pneumatic artificial muscle (h-PAM).

Several types of PAMs have been developed. Among these, braided muscles, also known as McKibben muscles, are commonly used at present [3][4]. Fig. 1 (a) illustrates the structure of a braided muscle, which is composed of a braided sleeve and a rubber tube. Upon pressurization of the tube, the helical angle of the fiber undergoes deformation. This process continues until the volume of the rubber tube reaches its maximum capacity, while maintaining the original helical length and the number of fibers turn constant.

Although the helical braided structure is advantageous for creating long, thin, and flexible muscles [5][6], it exhibits diminished contraction performance when the muscle's length is relatively short, a phenomenon referred to as the 'side effect' [7]. In its design, the muscle assumes a cylindrical shape. However, upon contraction, it tends to adopt a hemispherical shape at both ends. This deviation becomes more pronounced as the degree of contraction increases, further exacerbating the side effect.

Straight fiber muscles and pleated muscles are typically characterized by a cylindrical rubber tube reinforced with axial fibers [8][9], as shown in Fig. 1(b). These muscles can generate significant contraction force at the onset of contraction. Notably, a muscle with an extremely thin profile can achieve a maximum contraction of approximately 54.3% [10]. An additional advantage is the absence of friction during contraction, resulting in low hysteresis. However, when fully inflated, these muscles assume a spherical shape, and the presence of axial fibers restricts bending. These characteristic limits their applicability in scenarios that demand high flexibility.

The hyperboloid muscle featuring braided straight fibers, which assumes an hourglass-like shape in its relaxed state, is the focus of this study (Fig. 1(c)). Initially designed by H. M. Paynter [11][12], this muscle type contracts and adopts a spherical shape upon inflation. A notable feature is its relatively large internal diameter, allowing efficient gas flow for high-cyclic motion operations. The maximum contraction

ratio of this muscle is reported to be about 25%, with a contraction force of 500 N at 200 kPa, for a muscle measuring 2.5 cm in length and 1.25 cm in diameter. However, post-Paynter, there has been a lack of studies on this muscle, leaving its basic performance characteristics and design methodology somewhat unclear.

Knitted sleeve PAMs feature a shell constructed from knitted yarn [13][14]. These muscles are notable for their high contraction ratio, exceeding 50%, and their ability to produce a relatively constant force throughout most of their operational range. However, durability poses a significant challenge. Under tension, the yarns within the sleeve are prone to sharp bending, leading to sliding against each other. Furthermore, the knitted fabric is susceptible to snagging, resulting in the yarn being easily pulled out, forming loops.

Other varieties of PAMs without fiber reinforcement include pouch motors [15][16], origami-inspired artificial muscles [17][18], and bellows muscles [19]. These are mostly constructed from welded thermoplastic resin sheets, making them exceptionally lightweight. Typically, these muscles are actuated by either low positive pressure or negative pressure, rendering them well-suited for applications involving physical interaction or soft bionic motions.

In this study, we explored foundational knowledge about the h-PAM. In our investigation of the h-PAM, we identified several features that potentially differentiate it from other PAMs. Preliminary experiments suggest it could offer comparative advantages over shorter McKibben muscles in terms of contraction efficiency. Additionally, the design of h-PAM, characterized by its larger end areas, is thought to potentially enhance its responsiveness to pressurization and depressurization. Another aspect is its braided straight fiber design, which appears to provide a balance between structural flexibility when unpressurized and a degree of bending rigidity. This balance may help in achieving shape stability, a challenge for some PAMs that either achieve high flexibility but struggle to maintain their shape or maintain shape but exhibit limited flexibility. Our initial findings indicate that using stiffer fibers in a straight configuration could improve bending rigidity when depressurized while retaining flexibility.

Building upon these advantages, this study focused on the contraction characteristics of the h-PAM with simulation and tests. Through deformation simulations, the development of the first prototype (Fig. 2), and subsequent testing, we uncovered several novel characteristics: (i) The contraction ratio, radius expansion ratio, and contraction force can be modulated by altering two design parameters: the height-to-radius ratio and the offset angle of the fibers. (ii) The muscle's post-pressurization shape can vary from spherical to cylindrical or even snowman-like, depending on the relaxed conditions, with the radius of the braided fiber's middle portion becoming larger, smaller, or remaining the same as that of the ends. (iii) The muscle's braided structure and tapered middle enable it to bend easily, despite the large radius of the lid. This feature is distinct from other fiber-reinforced muscles, allowing the short h-PAM to achieve both high contraction and substantial structural flexibility.

The remainder of this paper is organized as follows:

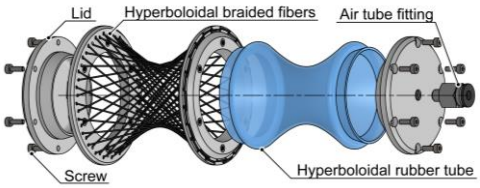

Fig. 3 Components of the h-PAM prototype.

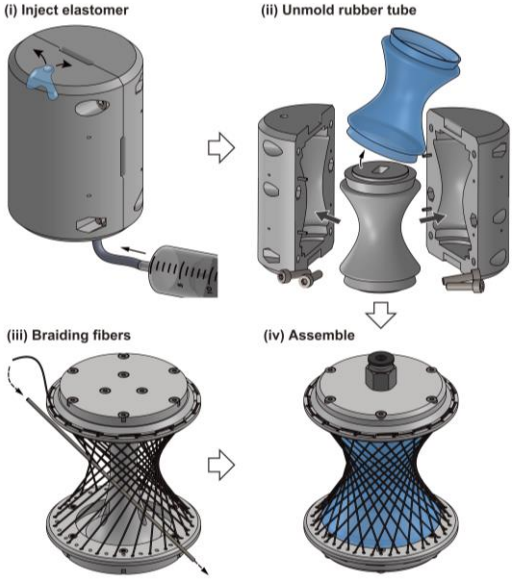

Fig. 4 Fabrication method of the h-PAM.

Section II details the fabrication method of the muscle. Section III presents the numerical analysis model and discusses the results related to the muscle's inflation behavior and contraction performance. Section IV demonstrates the actual motion of the prototype and examines the results concerning its contraction properties. Finally, Section VI concludes the paper, offering insights into potential future work.

II. Fabrication Method of the h-PAM Prototype

The initial prototype of the hyperboloidal pneumatic artificial muscle (h-PAM) was successfully fabricated, as depicted in Figure 3. The prototype comprises a hyperboloid-shaped rubber tube, an external hyperboloid-shaped braided shell, and lids at both ends to ensure structural integrity. The edges of the rubber membrane are tapered for a precise fit, and the membrane itself is securely sandwiched between 3D-printed components using bolts, forming an airtight seal.

Fig. 4 outlines the specific fabrication method for the h-PAM. The hyperboloidal rubber tubes were molded as shown in Fig. 4(i) and (ii), using a process where vacuum-defoamed liquid silicone rubber was injected into the mold from the bottom. The molds were produced using a Keyence AGILISTA-3200 3D printer with AR-M2 material. The fiber shell was braided by hand (Fig. 4(iii)), utilizing a jig and a specially designed part with holes to guide the fibers. Tension was applied during the braiding process, using a 1 mm diameter stainless steel pipe as a substitute for a traditional needle. This method facilitated the braiding process and reduced fiber friction, with the fibers themselves being made of a PTFE-coated (Ni-

TABLE 1 SIZE, MATERIALS AND PARAMETERS USED FOR THE MUSCLE SIMULATION

Muscle dimensions	$r = 25$ mm $h_{\max} = 50$ mm $\alpha = 60, 90, 120$ deg $t = 1$ mm
Fiber material	Nickel-titanium alloy wire (PTFE-coated) Diameter: 0.075 mm Young's modulus: $E_{\text{fiber}} = 60$ GPa Number of fibers incorporated: $N_{fiber} = 60$
Rubber tube material and Ogden model parameter [21]	Smooth-On, DragonSkin FX-Pro $\mu_1 = -0.1658, \alpha_1 = 3.275$ $\mu_2 = 0.4020, \alpha_2 = 3.309$ $\mu_3 = -0.2390, \alpha_3 = 3.275$
Lid material	Markforged, Onyx and carbon fiber

P-PTFE) Nickel-titanium alloy wire, 0.075 mm in diameter. The entire braiding process took approximately three hours for each muscle. Table 1 provides a detailed summary of the dimensions, materials, and parameters utilized in the muscle simulation in the next section.

III. SIMULATION MODEL

A. Basic Equations of the Muscle

PAMs are actuators that transform the volume expansion of a membrane, caused by gas pressure, into contraction motion. This expansion causes each fiber to bend, leading to the axial contraction of the entire shell.

Fig. 5 illustrates the structure of the shell and the actuation process of h-PAM. The surface of a one-sheet hyperboloid in this model is generated by rotating a straight-line asymptote around an axis. The hyperboloid surface of the muscle, denoted as $\boldsymbol{x}$, is represented parametrically as follows:

$$\boldsymbol{x} = \begin{pmatrix} \sqrt{h_{\max}^2 \tan^2\theta\,(s^2 - s) + r^2}\cos t \\ \sqrt{h_{\max}^2 \tan^2\theta\,(s^2 - s) + r^2}\sin t \\ h_{\max} s \end{pmatrix}. \tag{1}$$

Here, $h_{\max}$ is the height of the relaxed muscle, r is the radius at both ends of the muscle, θ is the braid angle of the fiber, and s $(0 \le s \le 1)$ and t $(0 \le t \le 2\pi)$ are parameter. The braid angle θ can be expressed in terms of the fiber's offset angle α as:

$$\theta = \operatorname{atan}\left(\frac{h_{\max}}{2r\sin\frac{\alpha}{2}}\right). \tag{2}$$

For simplicity, α is used in place of θ in subsequent subsections.

Considering the energy storage in the rubber membrane and neglecting energy loss due to friction, the stored energy in the muscle f, and contraction force F are calculated as:

$$f = pV - E_{\text{rubber}} - E_{\text{fiber}}. \tag{3}$$

$$F = -\frac{\mathrm{d}f}{\mathrm{d}h}. \tag{4}$$

Where p is the gauge pressure, V is the inner volume of the muscle, E_{rubber} is the potential energy of the rubber shell, E_{fiber} is the potential energy of the fibers, and h is the muscle height.

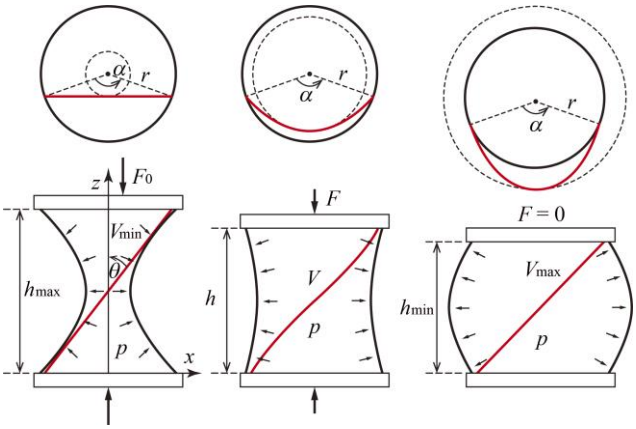

Fig. 5 Top view and the side view of the actuation process of h-PAM. The red line indicates the deformation process of a single fiber.

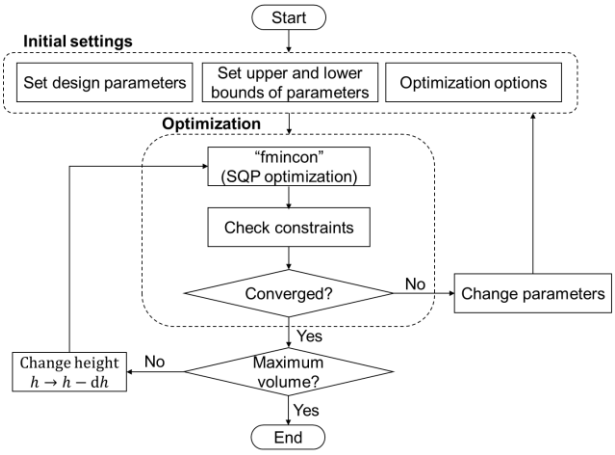

Fig. 6 Flow chart of the optimization.

A. Numerical Simulation for Deformation Analysis

1) Fmincon Method for Optimization Algorithm

In the context of h-PAMs, which contract while simultaneously increasing in volume, we assume quasi-static conditions where the muscle deforms into a stable shape at each specific height. To analyze this behavior, we employed an optimization approach to identify the minimum energy shape of the muscle.

This study utilizes the 'fmincon' method, widely recognized as a constrained non-linear optimization algorithm. The 'fmincon' method, an inbuilt function in MATLAB [20], is adept at handling such optimization problems. Through this method, we determined the unknown trajectory of the braided fiber. In this optimization framework, the total energy of the muscle, denoted as f, is treated as the objective function, with constraints applied to minimize this energy. A flow chart illustrating the basic process of this optimization is provided in Fig. 6, and a detailed explanation of the calculations is presented in the subsequent subsection.

2) Mathematical Model and Parameters

The braided shell of the muscle, being axially symmetrical, exhibits linear contraction without any torsional deformation. This implies that analyzing a single fiber is sufficient for our purposes.

Fig 7 illustrates a linkage model of a single fiber of the muscle shell. In this model, we neglect the thickness of the

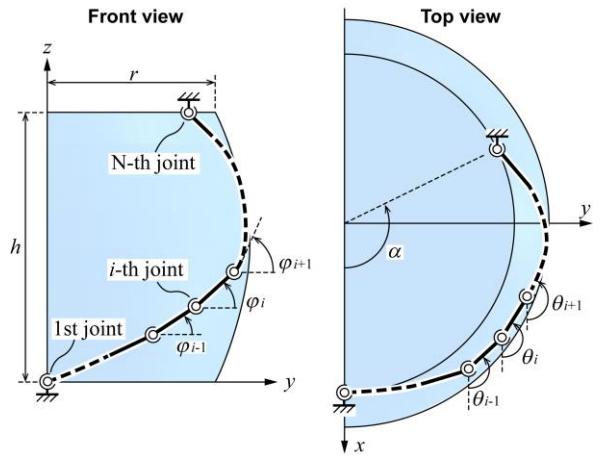

Fig. 7 Model of a single fiber in the h-PAM shell. Constant-length linkages are connected serially with ball joints.

fiber and any friction between fibers. Each fiber is modeled as consisting of $N-1$ linkages of length L, connected serially with N ball joints. L is calculated as follows:

$$L = \frac{\sqrt{h_{\max}^2 + \left\{2r\sin\left(\frac{\alpha}{2}\right)\right\}^2}}{N-1}. \tag{5}$$

Here, h (where $h_{\min} \le h \le h_{\max}$) represents the height of the muscle.

The coordinate system $(x, y, z)$of the model is defined as depicted in Fig. 7. The position of the joints $\boldsymbol{x}_i = (x_i, y_i, z_i)$ (for $i \in \mathbb{N}, 1 \le i \le N$) is determined by the azimuth angle θ_i, and the elevation angle φ_i, calculated as follows:

$$\begin{cases} \boldsymbol{x}_1 = \begin{pmatrix} r \\ 0 \\ 0 \end{pmatrix}, \\ \boldsymbol{x}_i = \begin{pmatrix} x_{i-1} + L\cos\varphi_{i-1}\cos\theta_{i-1} \\ y_{i-1} + L\cos\varphi_{i-1}\sin\theta_{i-1} \\ z_{i-1} + L\sin\varphi_{i-1} \end{pmatrix}, (2 \le i \le N). \end{cases} \tag{6}$$

Note that the constraints of $\boldsymbol{x}_N$ will be taken into account in equations (18), (19), and (20).

In the optimization process, the constrained minimization is utilized to determine the value of $\theta_1, \cdots, \theta_{N-1}, \varphi_1, \cdots, \varphi_{N-1}$. This means that $2(N-1)$ parameters are determined in the optimization.

3) Objective function

The 3D shape of the object, obtained by rotating the link between points $\boldsymbol{x}_i$ and $\boldsymbol{x}_{i+1}$ around the z-axis, forms a hyperboloid. However, if the link length is sufficiently short relative to the radius, this shape approximates a truncated cone. The volume of this truncated cone is geometrically calculated as follows:

$$V_i = \frac{\pi(z_{i+1} - z_i)}{3}\left(r_i^2 + r_i r_{i+1} + r_{i+1}^2\right). \tag{7}$$

Here, the radius of the ith joint, r_i is given by $r_i = \sqrt{x_i^2 + y_i^2}$.

Subsequently, we calculate the potential energy of the rubber shell. Assuming the volume of the shell material for the truncated cone can be determined by multiplying its lateral area with the thickness t. Using an N-dimensional Ogden model, the strain energy of rubber is expressed as:

$$E_{\text{rubber},i} = \pi\left(r_{\text{init},i} + r_{\text{init},i+1}\right)Lt\sum_{n=1}^{N}\frac{\mu_n}{\alpha_n}\left(\lambda_1^{\alpha_n} + \lambda_2^{\alpha_n} + \lambda_3^{\alpha_n} - 3\right). \tag{8}$$

Here, $r_{\text{init},i}$ is the radius of the ith joint in its initial state (before expansion), and L is the length of generating line of the truncated cone. The principal stretches $\lambda_1, \lambda_2,$ and λ_3 are defined as:

$$r_{\text{init},i} = \sqrt{x_{\text{init},i}^2 + y_{\text{init},i}^2}, \tag{9}$$

$$L = \sqrt{\left(r_{\text{init},i+1} - r_{\text{init},i}\right)^2 + \left(z_{\text{init},i+1} - z_{\text{init},i}\right)^2}, \tag{10}$$

$$\lambda_1 = \frac{r_i}{r_{\text{init},i}}, \tag{11}$$

$$\lambda_2 = \frac{z_{i+1} - z_i}{z_{\text{init},i+1} - z_{\text{init},i}}, \tag{12}$$

$$\lambda_3 = \frac{1}{\lambda_1 \lambda_2}. \tag{13}$$

Next, we calculate the potential energy of the wire. If the ith link is considered to be curved with angle $\varphi_i - \varphi_{i-1}$ with a constant curvature, the strain energy of the wire due to the bending moment can be approximated as follows.

$$E_{\text{fiber},i} = \frac{E_{\text{fiber}} I_{\text{fiber}} (\varphi_i - \varphi_{i-1})^2}{2L}. \tag{14}$$

Here, E_{fiber} is the Young's modulus of the wire and I_{fiber} is the wire's second moment of area. Also, since the wire ends are fixed at the angle θ, the calculation is performed using $\varphi_0 = \varphi_N = \theta$.

The objective function f_{obj} is derived by summing the terms V_i, $E_{\text{rubber},i}$ and $E_{\text{fiber},i}$ as follows.

$$f_{\text{obj}} = \sum_{i=1}^{N-1}\left(V_i - E_{\text{rubber},i}\right) - N_{\text{fiber}}\sum_{i=1}^{N} E_{\text{fiber},i}. \tag{15}$$

Here, N_{fiber} is the number of fibers.

4) Bound Constraints

The azimuth angle θ_i of the first link, understandably, does not rotate towards the radial direction $0 < \theta_1$. Similarly, for the (N-1) th link $\theta_{N-1} < \alpha + \pi$. Therefore, considering that the azimuth angles of all links fall within these minimum and maximum values, the bound constraints for the azimuth angle are defined as:

$$0 < \theta_i < \alpha + \pi. \tag{16}$$

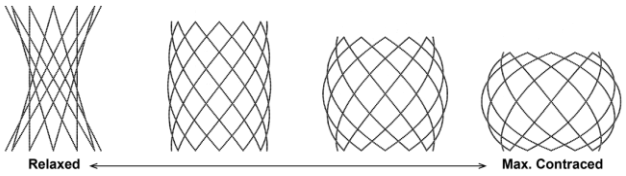

Fig. 8 Deformation process of an h-PAM. Transition from relaxed to maximum contracted state, with parameters $h/r = 3.0$ ($h = 30, r = 10$), $\alpha = 120$ deg, $t = 0$, and $N = 30$.

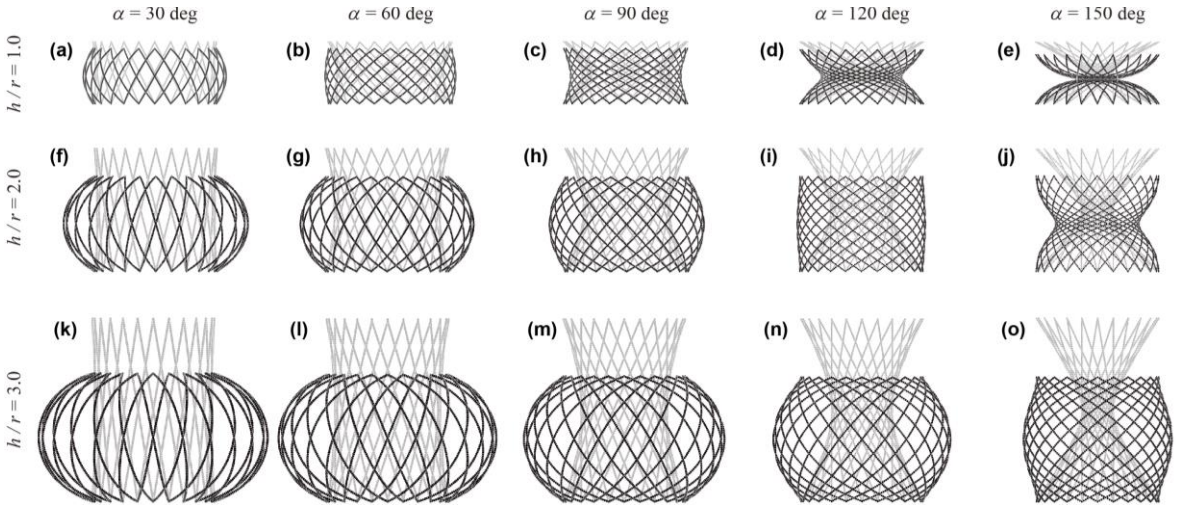

Fig. 9 Relaxed and contracted state of the h-PAMs with different parameters

Furthermore, the bound constraints for the elevation angle φ_i are set to encompass all possible ranges:

$$-\frac{\pi}{2} \leq \varphi_i \leq \frac{\pi}{2}. \tag{17}$$

5) Nonlinear Equality Constraints

In the model, the N-th joint of the fiber is anchored at the muscle end, which possesses a radius r and an offset angle α. Consequently, the following constraints are applied:

$$x_N^2 + y_N^2 - r^2 = 0. \tag{18}$$

$$\operatorname{atan}\left(\frac{y_N}{x_N}\right) - \alpha = 0. \tag{19}$$

Additionally, when incorporating the height h constraint for the N-th joint, we consider:

$$z_N - h = 0. \tag{20}$$

It is important to note that Equation (20) is not factored into the constraints when calculating the muscle's maximum contraction. However, it is included when assessing the muscle's state during contraction.

B. Results

In the optimization process, Sequential Quadratic Programming (SQP) was selected as the algorithm of choice due to its efficiency in speed optimization. The 'MaxIterations' parameter, defining the upper limit of solver iterations, was set at 10,000. Similarly, 'MaxFunctionEvaluations', which limits the number of function evaluations, was set at 100,000. The total number of joints, N, in the model was fixed at 30.

The presence of a large number of unknown parameters indeed poses a challenge in optimization. To efficiently solve the optimization problem, we set the initial values to the optimal values from the previous iteration, and we were able to efficiently solve the optimization problem. This approach can be used because the optimization is done by incrementally changing the muscle height parameter h. This approach ensured that the initial values were close to the optimal, improving convergence speed, increasing the posibility of converging to a solution near the global optimum, and reducing computational errors.

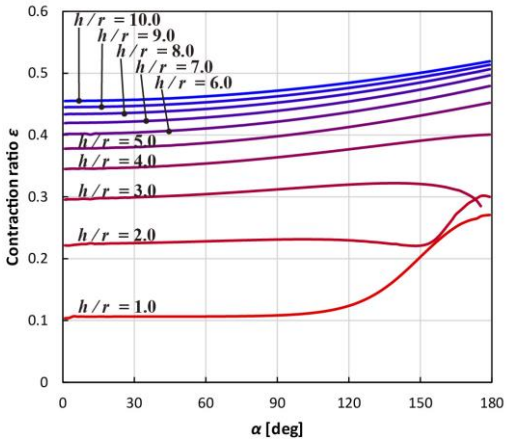

Fig. 10 Relationship between the offset angle α and contraction ratio ε under various aspect ratio h/r. Parameters: $t = 0$, and $N = 30$.

Fig. 8 illustrates an example of the muscle's deformation process when the thickness of the rubber shell, t is zero. The results indicate significant expansion in the middle part of the muscle, leading to a spherical shape of the shell. Notably, slippage between fibers was observed, a factor that could introduce resistance forces counteracting the actuation, predominantly due to fiber friction. This phenomenon could result in mechanical hysteresis. Therefore, the use of a more slippery fiber material is suggested to facilitate larger deformation without significant resistance.

Fig. 9 shows the relaxed and contracted states of the h-PAMs under varying parameters, highlighting how the offset angle α significantly influences the ideal deformation shape post-pressurization. With a smaller offset angle α, same as general straight fiber muscles [10], the braided shell adopts a pumpkin-like shape upon contraction (characterized by a rectangular cross-section with rounded corners and a full radius) and expands to a larger diameter. In such scenarios, the reduced density of the braiding raises concerns regarding pressure resistance.

Conversely, with an increased offset angle α, the expansion of the shell's middle section diminishes. In cases where the aspect ratio is small and the offset angle α is

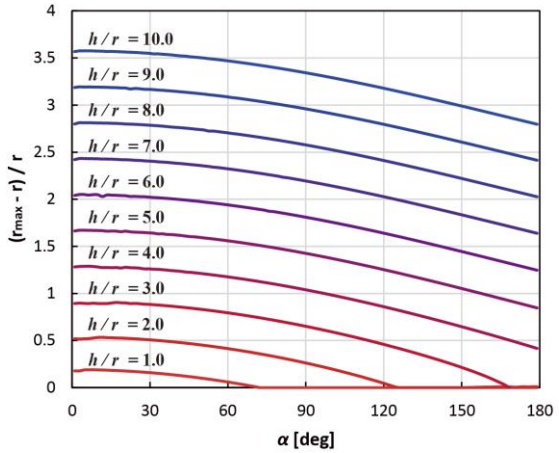

Fig. 11 Relationship between the offset angle α and expansion ratio under various aspect ratio h/r. Parameters: $r = 10$, $t = 0$, and $N = 30$.

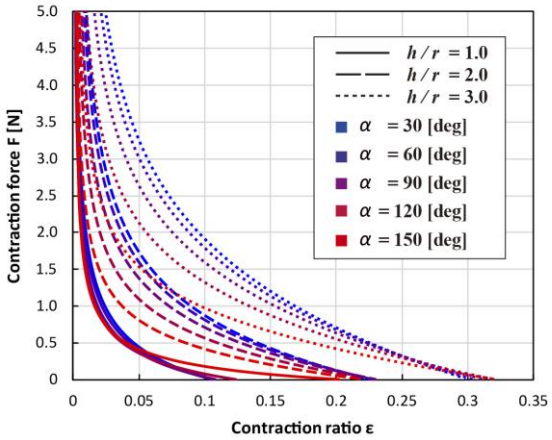

Fig. 12 Relationship between the contraction ratio ε and contraction force F under various aspect ratio h/r and offset angle α. Parameters: $r = 10$ mm, $t = 0$ mm, $N = 30$, and $p = 1$ kPa.

large, the muscle may assume a snowman-like shapein its contracted state, as illustrated in Fig. 9(d), (e), and (j).

Fig. 10 presents the simulated relationship between the offset angle α and the contraction ratio $\varepsilon = (h_{\max} - h_{\min})/h_{\max}$ across various aspect ratio h/r. Interestingly, while the contracted state's shape is heavily influenced by the offset angle α, the contraction ratio undergoes only minor changes.

When the aspect ratio increased while maintaining a constant offset angle α, the contraction ratio monotonically increased. As both the aspect ratio and offset angle increased, the contraction ratio approached 54.3%, aligning with results observed in straight fiber muscles [10]. Additionally, for aspect ratios less than 2.0 combined with offset angles exceeding 120 degrees, the muscle exhibited hourglass-shaped deformation, with the contraction rate large rising with the offset angle.

Fig. 11 shows the simulated results that plot the relationship between the offset angle α and expansion ratio $(r_{\max} - r)/r$ across various aspect ratios h/r. Here, $r_{\max}$ denotes the radius of the muscle at its widest point during contraction. Notably, an expansion ratio of zero indicates that the muscle's diameter remains unchanged from its relaxed state even in the contracted state.

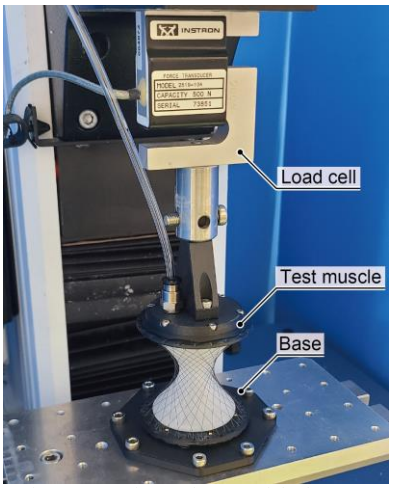

Fig. 13 Experimental setup of the h-PAM.

Furthermore, the expansion ratio exhibited a linear increase when the aspect ratio increased, with the offset angle held constant. This expansion ratio should be carefully designed, taking into account the elongation limits of the rubber material. As the offset angle increased, the expansion ratio decreased, attributed to the initial hourglass shape effect. It was also observed that at an aspect ratio of 3.0 or less, certain offset angles resulted in an expansion ratio of 0. This finding is pivotal in designing slender muscles and minimizing diameter increase during muscle contraction.

Fig. 12 illustrates the simulated results, showing the relationship between the contraction ratio ε and contraction force F across various aspect ratio h/r and offset angle α. In these simulations, the muscle radius was set at $r = 10$ mm and the applied pressure at $p = 1$ kPa.

Mirroring the behavior of straight-fiber muscles, the model predicts that at a contraction ratio of zero, the contraction force theoretically approaches infinity [10]. As the contraction ratio increases, there is a notable decrease in the contraction force. Additionally, the results indicate that the contraction force increases with an increasing aspect ratio and decreases with an increasing offset angle.

IV. Measurement of h-PAM Characteristics

A. Contraction Measurements of h-PAM

Observations and measurements were conducted on the first h-PAM prototype to assess its contraction characteristics under pressurization. The muscle was affixed to a tensile testing machine (INSTRON, Model 3343), and pressure was applied as illustrated in Fig. 13. The contraction experiment followed this procedure:

(i) The origin was set at the point where the contraction force equals zero at zero pressure.
(ii) A constant pressure was then applied to the h-PAM.
(iii) The h-PAM was contracted at a rate of 1 mm/s until the contraction force becomes zero.
(iv) It was then extended at 1 mm/s back to the origin.
(v) Steps (iii) and (iv) were repeated for a total of 10 measurements.
(vi) Subsequently, the pressure was varied, and steps (iii), (iv), and (v) were repeated.

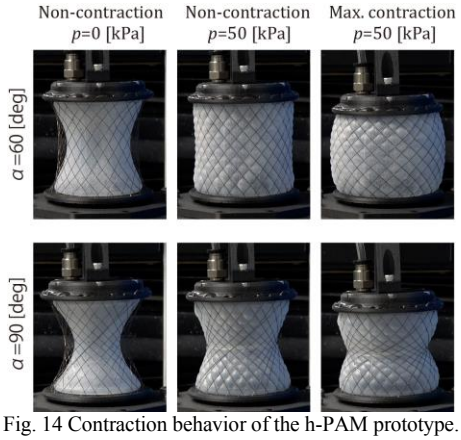

Fig. 14 Contraction behavior of the h-PAM prototype.

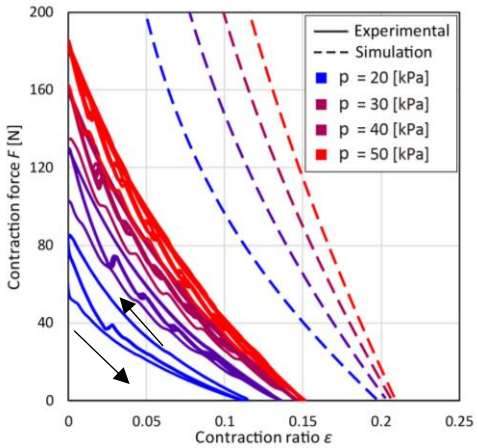

Fig. 15 Relationship between the contraction ratio ε and contraction force F of the h-PAM. Dashed lines represent simulation results and solid lines indicate the measured results. Parameters: $r = 25$ mm, $h_{\max} = 50$ mm, $\alpha = 60$ deg t=1 mm, N=30.

Figure 14 demonstrates the appearance of the h-PAM with offset angles of 60 and 90 degrees before and after applying a pressure of 50 kPa. In comparison with the simulation results shown in Figures 7(g) and (h), the muscle did not expand as anticipated. Notably, with increasing offset angle α, the expansion was less pronounced, likely due to the friction between fibers. Consequently, utilizing materials with a thin lower coefficient of friction or incorporate non-braided structure might be a viable solution to achieve larger deformation.

Additional observations revealed that the rubber tube, with an offset angle of 90 degrees, experienced buckling during contraction. This buckling phenomenon, which impedes radial expansion of the tube, is presumably due to the rubber's softness and the minimal cross-sectional secondary moment at the tube's narrowest diameter in the center of its hourglass shape.

Fig. 15, and 16 present both simulated and measured data on contraction forces and ratios under various pressures for h-PAMs with two different offset angles.

Fig. 15 illustrates the results for an offset angle α of 60 degrees. The graph indicates that, when accounting for strain in the rubber tubing, the maximum contraction rate increases with elevated pressure. Notably, at a pressure of 50 kPa, the initial maximum contraction force was measured at 184 N, with a maximum contraction ratio

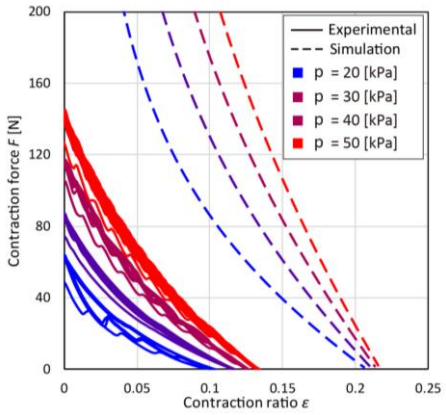

Fig. 16 Relationship between the contraction ratio ε and contraction force F of the h-PAM. Dashed lines represent simulation results and solid lines indicate the measured results. Parameters: $r = 25$ mm, $h_{\max} = 50$ mm, $\alpha = 90$ deg t=1 mm, N=30.

of 15.1% – approximately 75% of the simulated value. The discrepancy in contraction and elongation trajectories is attributed to the hysteresis effects in the rubber and fiber.

Fig. 16 display the results for offset angles of 90. The experimental outcomes were also lower than those predicted by the simulations. As observed in Figure 14, the muscle did not expand to the extent anticipated in the simulations. As discussed, we identified that a large offset angle necessitates certain modifications to address the observed issues, such as altering the surfaces of the fiber and rubber tubing to more slippery materials. This adaptation is crucial for improving the muscle's performance.

Additionally, as the muscle was handmade, which may have led to deviations from the ideal shape due to loosened or bent fibers, potentially resulting in reduced initial force and contraction. Future efforts will focus on revising the fabrication process and structure to enhance performance.

B. Contraction Test of a McKibben Actuator

Next, the maximum shrinkage of the McKibben actuator was measured for comparison. The diameter and length of the muscle are 50 mm and 50 mm, respectively. A nylon mesh tube with a braid angle of 25 degrees was placed on the outside of a natural rubber tube with an outer diameter of 50 mm and a thickness of 1 mm, and both ends were sealed with a 5.5 mm thick MDF lid.

When a pressure of 50 kPa was applied, the actuator contracted by 3.0 mm with a contraction ratio of 6.0% without load (Fig. 17). Compared to this result, the h-PAM, which contracted by 15%, contracted by 2.5 times.

Generally, McKibben actuators have a contraction ratio of about 20%. However, when the length of the actuator is extremely short, as in this configuration, the proportion of the non-deforming parts to the overall length becomes larger, so the effect of the restraints at both ends that inhibited expansion [7] may have increased, resulting in a lower contraction ratio.

A. Bending Test of h-PAM

Furthermore, to assess the flexibility of the h-PAM, we conducted bending tests. Generally, braided muscles, like

Fig. 17 Contraction behavior of a McKibben actuator (0 to 50 kPa).

Fig. 18 Bending test demonstrating the flexibility of the muscle.

those shown in Fig. 1, exhibit large deformability, whereas straight fibers, as depicted in Fig. 1(b), are structurally more resistant to bending when fiber is stiff.

Fig. 18 illustrates the h-PAM bent. Despite combining elements of both braided and straight fiber structures, the h-PAM demonstrated adequate flexibility. This finding highlights the h-PAM's versatile design, capable of maintaining bendability even with its hybrid structural composition.

V. Conclusion

In this paper, we introduced a hyperboloidal pneumatic artificial muscle (h-PAM), featuring a rubber tube reinforced by hyperboloidal braided straight fibers. Our simulations and experiments have demonstrated that this structure possesses the flexibility and bendability characteristic of braided fiber muscles, while also capable of generating substantial contraction forces akin to straight fiber muscles in the initial stages of contraction.

To increase the contraction force or ratio, enlarging the fiber shell and utilizing fine fiber or rubber with a lower coefficient of friction, or building with a non-braided structure would be beneficial. Additionally, increasing the operating pressure would require the use of stretchable, yet durable rubber materials.

Although h-PAM may not be ideal for creating long structures with small diameters, it is well-suited for constructing larger diameter, shorter length structures. This makes it particularly apt for configurations where multiple muscles are connected in series, offering potential applications in the development of worm robots or soft manipulators.

Future work will focus on developing a more advanced simulation model that accurately replicates the behavior of actual muscles, even at increased offset angles. This model will incorporate considerations for the friction between fibers and rubber, further enhancing the accuracy and applicability of our h-PAM design. Additionally, we aim to extend our research to include the modeling and measurement of bending stiffness, providing a comprehensive comparison with other PAM technologies. This will enable a deeper understanding of the mechanical properties of h-PAM and its potential advantages over existing solutions. By exploring these avenues, we anticipate contributing significantly to the field of soft robotics, particularly in the optimization and application of pneumatic artificial muscles.

Acknowledgment

We greatly acknowledge the support of the Fluid Power Technology Promotion Foundation.

References

[1] J. Walker, T. Zidek, C. Harbel, S. Yoon, F. S. Strickland, S. Kumar, and M. Shin, “Soft robotics: A review of recent developments of pneumatic soft actuators”, *Actuators*, vol. 9, no. 1, pp. 1–26, Jan. 2020.

[2] F. Daerden and D. Lefeber, “Pneumatic artificial muscles: actuators for robotics and automation”, *European Journal of Mechanical and Environmental Engineering*, vol. 47, no. 1, pp. 11–21, 2002.

[3] B. S. Kang, C. S. Kothera, B. K. Woods, and N. M. Wereley, “Dynamic modeling of McKibben pneumatic artificial muscles for antagonistic actuation”, 2009 *IEEE International Conference on Robotics and Automation*, pp. 182–187, May 2009.

[4] B. Tondu, V. Boitier, and P. Lopez, “Naturally compliant robot-arms actuated by McKibben artificial muscles”, *the IEEE International Conference on Systems, Man, and Cybernetics*, vol. 3, pp. 2635–2640, Oct. 1994.

[5] E. G. Hocking and N. M. Wereley, “Analysis of nonlinear elastic behavior in miniature pneumatic artificial muscles”, *Smart Materials and Structures*, vol. 22, no. 1, pp. 1–14, 2012.

[6] S. Kurumaya, H. Nabae, G. Endo, and K. Suzumori, “Design of thin McKibben muscle and multifilament structure”, *Sensors and Actuators A: Physical*, vol. 261, pp. 66–74, Jul. 2017.

[7] B. Tondu and P. Lopez, “Modeling and control of McKibben artificial muscle robot actuators”, *IEEE Control Systems Magazine*, vol. 20, no. 2, pp. 15–38, Apr. 2000.

[8] T. Nakamura and H. Shinohara, “Position and force control based on mathematical models of pneumatic artificial muscles reinforced by straight glass fibers”, *the 2007 IEEE International Conference on Robotics and Automation*, pp. 4361–4366, Apr. 2007.

[9] D. Villegas, M. Van Damme, B. Vanderborght, P. Beyl, and D. Lefeber, “Third-generation pleated pneumatic artificial muscles for robotic applications: Development and comparison with McKibben muscle,” *Advanced Robotics*, vol. 26, no. 11-12, pp. 1205-1227, Jul. 2012.

[10] F. Daerden and D. Lefeber, “The concept and design of pleated pneumatic artificial muscles”, International Journal of Fluid Power, vol. 2, no. 3, pp. 41–50, 2001.

[11] H. M. Paynter, “Hyperboloid of revolution fluid-driven tension actuators and method of making”, US4721030, 1988.

[12] H. M. Paynter, “High pressure fluid-driven tension actuators and methods for constructing them”, US4751869, 1988.

[13] B. Jamil, S. Lee, and Y. Choi, “Conductive knit-covered pneumatic artificial muscle (k-PAM) actuator”, *2018 IEEE/RSJ International Conference on Intelligent Robots and Systems*, pp. 1476–1481, Oct. 2018.

[14] A. Maziz, A. Concas, A. Khaldi, J. Stålhand, N. K. Persson, and E. W. Jager, “Knitting and weaving artificial muscles”, *Science Advances*, vol. 3, no. 1, pp. 1–11, Jan. 2017.

[15] R. Niiyama, X. Sun, C. Sung, B. An, D. Rus, and S. Kim, “Pouch motors: Printable soft actuators integrated with computational design”, *Soft Robotics*, vol. 2, no. 2, pp. 59–70, Jun. 2015.

[16] N. Oh, Y. J. Park, S. Lee, H. Lee, and H. Rodrigue, “Design of paired pouch motors for robotic applications”, *Advanced Materials Technologies*, vol. 4, no. 1, pp. 1–9, Oct. 2019.

[17] S. Li, D. M. Vogt, D. Rus, and R. J. Wood, “Fluid-driven origami-inspired artificial muscles”, *the National Academy of Sciences*, vol. 114, no. 50, pp. 13132–13137, Dec. 2017.

[18] J. G. Lee and H. Rodrigue, “Origami-based vacuum pneumatic artificial muscles with large contraction ratios”, *Soft Robotics*, vol. 6, no. 1, pp. 109–117, Feb. 2019.

[19] W. Felt, M. A. Robertson, and J. Paik, “Modeling vacuum bellows soft pneumatic actuators with optimal mechanical performance”, *2018 IEEE International Conference on Soft Robotics*, pp. 534-540, Apr. 2018.

[20] K. Kusakana, “Minimum cost solution of isolated battery-integrated diesel generator hybrid systems”, *South African University Power and Energy Conference*, pp. 141-147, Jan. 2015.

[21] L. Marechal, P. Balland, L. Lindenroth, F. Petrou, C. Kontovounisios, and F. Bello, “Toward a common framework and database of materials for soft robotics”, *Soft Robotics*, vol. 8, no. 3, pp. 284-297, Jun. 2021.